

Research Article

Open Access

Alfonso Pedone*, Francesco Muniz-Miranda, Antonio Tilocca, and Maria Cristina Menziani

The antioxidant properties of Ce-containing bioactive glass nanoparticles explained by Molecular Dynamics simulations

DOI 10.1515/bglass-2016-0003

Received Dec 05, 2015; revised Mar 24, 2016; accepted Apr 02, 2016

Abstract: Molecular dynamics simulations of two glass nanoparticles with composition $25\text{Na}_2\text{O}\cdot 25\text{CaO}\cdot 50\text{SiO}_2$ mol% (Ce-K NP) and $46.1\text{SiO}_2\cdot 24.4\text{Na}_2\text{O}\cdot 26.9\text{CaO}\cdot 2.6\text{P}_2\text{O}_5$ mol.% (Ce-BG NP) doped with 3.6 mol% of CeO_2 have been carried out in order to explain the enhanced antioxidant properties of the former glass with respect to the latter.

The present models show that the different catalase mimetic activity of the two NPs is related to the $\text{Ce}^{3+}/\text{Ce}^{4+}$ ratio exposed at their surface. In fact, this ratio is about 3.5 and 13 in the bulk and at the surface of the Ce-BG NP, and 1.0 and 2.1 in the bulk and at the surface of the Ce-K NPs, respectively. Since both oxidation states are necessary for the catalysis of the dismutation reaction of hydrogen peroxides, NPs with a very high $\text{Ce}^{3+}/\text{Ce}^{4+}$ ratio possess poorer antioxidant properties.

Moreover, our simulations reveal that the already low silicate connectivity found in the bulk glasses examined here is further reduced on the nanoparticle surface, whereas the $\text{Na}^+/\text{Ca}^{2+}$ ratio rapidly increases. Sodium, calcium and cerium sites in proximity of the surface are found to be under-coordinated, prone to quickly react with water present in physiological environments, thus accelerating the glass biodegradation

1 Introduction

Bioactive glasses are widely employed in clinical applications for repair and replacement of diseased and damaged bone tissues. Once implanted in the body, in contact with the physiological fluids, a rapid sequence of chemical reactions leads to the formation of a hydroxycarbonate apatite (HCA) layer on the glass surface. HCA is similar to bone mineral; it interacts with collagen fibrils to integrate with the host bone, giving rise to a strong chemical interface [1, 2].

Bioglass 45S5 [3] (24.5% Na_2O -24.5% CaO -45.0% SiO_2 -6% P_2O_5 by weight) bonds with bone rapidly and its dissolution products, *i.e.* soluble silica and calcium ions, stimulate osteogenic cells to produce bone matrix [4, 5] away from the bone-implant interface.

In order to improve the physical-chemical properties and therapeutic benefits of conventional bioactive glasses, several additional elements have been incorporated into the silicate matrix. For example, Ag, Ce, Zn and F ions have been employed to confer antibacterial properties to bioactive glasses [16–23], whereas the addition of Ga ions has been shown to be beneficial to cure hypercalcemia associated with bone tumour metastasis [24] and to prevent bacterial growth [25].


Nanosized bioactive glass particles represent an attractive alternative to glass micro-sized particles for hard tissue regeneration [6]. Their small particle size and large surface area lead to higher bioactivity [6, 7], rapid remineralization [8], enhanced interaction with fibrinogen and cell proliferation [9] and improved mechanical properties [10].

Recently, it has been shown that cerium oxide nanoparticles (nanocerium) exhibit superoxide dismutase (SOD) and catalase mimetic activities and can potentially be used to treat diseases associated with oxidative stress [11]. This activity is strictly related to the simultaneous presence of Ce^{3+} and Ce^{4+} at the glass surface, which are able to catalyse the dismutation reaction of hydrogen peroxide as also demonstrated in CeO_2 nanoparticles [12].

*Corresponding Author: **Alfonso Pedone:** Dipartimento di Scienze Chimiche e Geologiche, Università di Modena e Reggio Emilia, via G. Campi 183, Modena, 41125, Italy; Email: alfonso.pedone@unimore.it

Francesco Muniz-Miranda, Maria Cristina Menziani: Dipartimento di Scienze Chimiche e Geologiche, Università di Modena e Reggio Emilia, via G. Campi 183, Modena, 41125, Italy

Antonio Tilocca: Department of Chemistry and Thomas Young Centre, University College London, London WC1H 0AJ, UK

 © 2016 A. Pedone *et al.*, published by De Gruyter Open.

This work is licensed under the Creative Commons Attribution-NonCommercial-NoDerivs 3.0 License.

In fact, Ce^{3+} is able to reduce H_2O_2 to H_2O and, at the same time, Ce^{4+} is able to oxidize it first to HOO^\cdot and then to O_2 by following the reaction mechanism proposed by Celardo *et al.* [13].

Evidence of catalase mimetic activity in bulk $\text{Ce}^{3+}/\text{Ce}^{4+}$ doped bioglasses has also been reported by some of us [14]. However, the kinetics of the dismutation reactions is negatively influenced by the presence of phosphate units in the glass and/or in the physiological solution in which the catalase mimetic activity tests are carried out, owing to the formation of an amorphous insoluble phase ($\text{Ce}_2\text{O}_3 \cdot \text{CePO}_4$) [15, 16]. In fact, the P-free ternary soda-lime silicate bioactive glasses with composition 25 Na_2O 25 CaO 50 SiO_2 mol% proposed by Kokubo [17] exhibit a higher catalase mimetic activity when doped with the same amount of CeO_2 (3.6 mol%) [18].

Although an increased CeO_2 content in the glass compositions could in principle enhance their anti-oxidant ability, Ce concentrations above 5.3 mol% drastically reduce the bioactivity [16]. The enhanced dissolution rate, higher protein adsorption and faster apatite formation [19, 20] of glass nanoparticles could then be exploited in this context, by incorporating CeO_2 in bioactive glass nanoparticles instead of bulk glasses.

Molecular Dynamics (MD) simulations represent an increasingly common and powerful tool to access atomic-scale properties of nanosized materials including glasses [21, 22], aiding the interpretation of experimental trends. In this work, we have used classical MD simulations to generate two realistic nanosized models of 45S5 Bioglass[®] (BG NP) and Kokubo's P-free soda lime silicate glass (K NP), both doped with CeO_2 , in order to rationalize the bioactivity and different anti-oxidant properties of the two compositions.

2 Computational Details

Two structural models of BG and K NPs containing about 10000 atoms were generated by classical Molecular Dynamics (MD) simulations using the DL_POLY 2.14 package [23]. The $\text{Ce}^{4+}/\text{Ce}^{3+}$ ratio of each glass composition was fixed accordingly to experimental estimates: 25:75 for BGNP [14] and 46:54 for KNP [18]. The exact compositions of the two nanoparticles are reported in Table 1.

The adiabatic core-shell model [24] was adopted to treat explicitly the polarizability of O^{2-} ions, where a core bearing most of the atomic mass and a positive charge interacts with a negatively charged shell through a harmonic potential. This treatment leads to reliable reproductions

Table 1: Atomic composition of the two nanoparticles.

	Ce-BG	Ce-K
Ce^{4+}	27	60
Ce^{3+}	96	90
Na^+	1659	1754
Ca^{2+}	918	876
P^{5+}	177	
O	5528	5486
Si	1570	1754
tot	9975	10020

of the Q^n distributions of network former cations [25], enabling the computational study of the medium-range order of a nanoparticle at accessible computational costs. In fact, the same computational framework has been previously applied to model an undoped 45S5 BG nanoparticle [26]. A detailed description of the force-field functional forms used is reported in refs. [14, 27, 28] whereas the complete list of parameters is reported in Table 2.

As no periodic boundary conditions (PBCs) were applied in order to model an isolated nanoparticle, electrostatic forces were calculated through direct Coulomb sum, with a distance cut-off large enough to include all atomic pairs in the system, whereas van der Waals forces act within a cut-off of 8.0 Å.

The glass nanoparticles were generated following a computational procedure similar to that used in a previous work to generate glass nanofibers [29]. For each composition, the starting configuration was a cubic box of side ~ 52 Å generated from a (periodic) bulk simulation. This value was chosen in order to obtain a nanoparticle with radius of about 32–33 Å. After removing the PBCs, a spherical containing external field was imposed to the equilibrated system at 3200 K until a nanoparticle (NP) having a density close to the one of corresponding bulk systems [14] was obtained. (BGNP: 2.911 g/cm³; KNP: 2.851 g/cm³).

The functional form of the spherical containing external potential is:

$$F = \frac{A}{(R_0 - r)^6} \quad r > R_{cut}$$

At 3200 K we used $A = 100 \text{ eV} \cdot \text{Å}^5$, $R_0 = 40$ Å and $R_{cut} = 30$ Å for the first 50 ps and $A = 100 \text{ eV} \cdot \text{Å}^5$, $R_0 = 38$ Å and $R_{cut} = 29$ Å for the second 50 ps.

Then, maintaining the external spherical potential, the NP was kept at 3000 K for another 100 ps, then cooled to 300 K at a rate of $-5 \text{ K} \cdot \text{ps}^{-1}$ following the same melt-quench approach usually employed for bulk simu-

Table 2: Shell model interatomic potential: analytic functions and parameters. Atomic charges are reported as superscript text.

Potential forms and parameters			
Buckingham $Ae^{-r/\rho} - C/r^6$			
	A (eV)	ρ (Å)	C (eV Å ⁶)
$O_s^{-2.8482}-O_s^{-2.8482}$	22764.30	0.149000	27.88
$Si^{4+}-O_s^{-2.8482}$	1283.91	0.320520	10.66
$P^{5+}-O_s^{-2.8482}$	1120.0913	0.334772	0.0
$Ca^{2+}-O_s^{-2.8482}$	2152.3566	0.309227	0.09944
$Na^{1+}-O_s^{-2.8482}$	56465.345	0.193931	0.0
$Ce^{3+}-O_s^{-2.8482}$	2893.3405	0.323317	0.0
$Ce^{4+}-O_s^{-2.8482}$	4521.6365*	0.306140	0.0
Three-body potential $\frac{1}{2}k_b(\theta - \theta_0)^2 \exp(-[r_{12}/\rho + r_{13}/\rho])$			
	k_b (eV rad ⁻²)	θ_0 (deg)	ρ (Å)
$O_s^{-2.8482}-Si^{4+}-O_s^{-2.8482}$	100.0	109.47	1.0
$O_s^{-2.8482}-P^{5+}-O_s^{-2.8482}$	50.0	109.47	1.0
Core-shell spring potential $1/2k_s r^2$			
	k_s (eV Å ⁻²)	$Y(e)$	
$O_c^{+0.8482}-O_s^{-2.8482}$	74.92	-2.8482	

Note that the value of this parameter reported in ref. [28] of 45241.6365 eV was not correct.

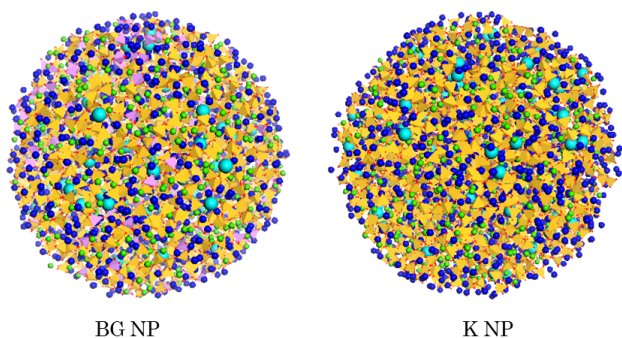


Figure 1: Snapshots of the final structures of the Ce-BG and Ce-K nanoparticles after the NVE production run. Silicate and phosphate ions are represented in yellow and violet tetrahedra, Na in blue spheres, Ca in green spheres, and Ce ions in cyan spheres.

lations [30]. At this stage, we used the parameters $A = 100 \text{ eV} \cdot \text{Å}^5$, $R_0 = 36 \text{ Å}$ and $R_{cut} = 28 \text{ Å}$.

A further constant-temperature equilibration run of 200 ps at 300 K was carried out with no applied external field and using a Berendsen thermostat [31] with a relaxation constant of 0.2 ps.

A final microcanonical (*i.e.* NVE) run of 240 ps at an average temperature of 300 K completed the simulation. During the temperature quenching and the following microcanonical run, the NPs maintained an overall spherical shape, with ratios between moments of inertia < 1.1 ,

and ellipsoid of inertia close to each other within a 0.5 Å threshold. Structural analysis was carried out on all configurations extracted from the microcanonical trajectory, sampled every 0.4 ps. Two independent samples were obtained for each composition.

3 Results and Discussions

The final structures of two of the Ce-BG and Ce-K NPs models generated are reported in Figure 1.

The final densities, computed after the relaxation at 300 K, were 2–3% lower than the experimental values of the bulk for both the NPs, denoting slightly less compact structures.

These structures have been characterized in terms of relative and absolute distribution of the ions from the center of mass, in order to better highlight how the chemical composition changes from the cores of the NPs toward their surfaces, in analogy to previous work [26].

Figure 2 shows the density (ρ_i), and fraction (χ_i) profiles of each ionic species i ($i = \text{Na, Ca, Ce}^{3+/4+}, \text{Si, P and O}$) with the distance (R) from the center of mass of the NP.

The profiles were calculated by dividing the volume of the NPs in concentric spherical shells of thickness $\Delta R =$

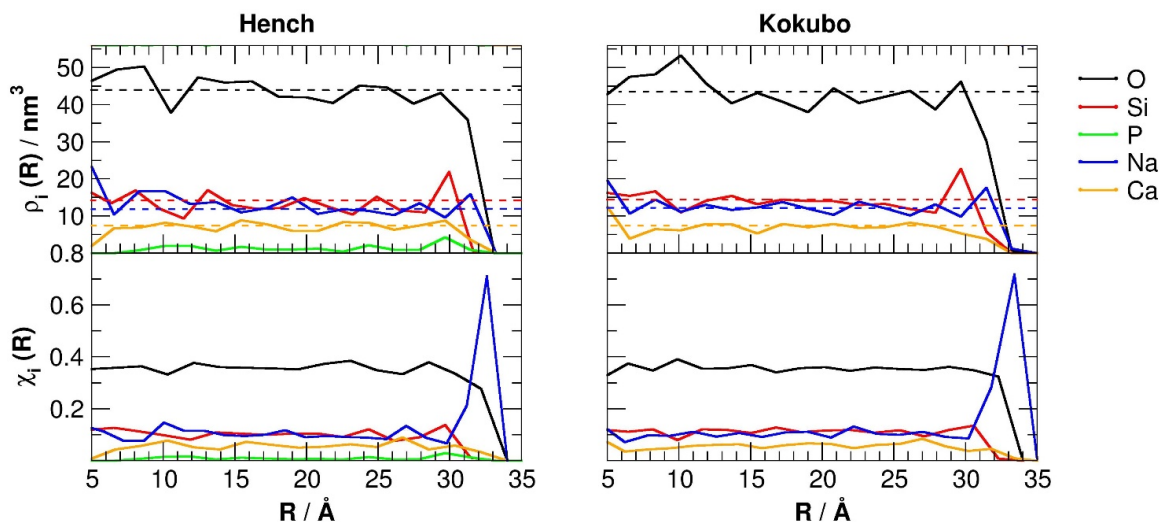


Figure 2: Number density $\rho_i(R)$ (middle) and fraction $\chi_i(R)$ (bottom panel) of different species as a function of their distance from the centre of mass of the nanoparticles. Dashed lines mark the corresponding number density of each species in the bulk.

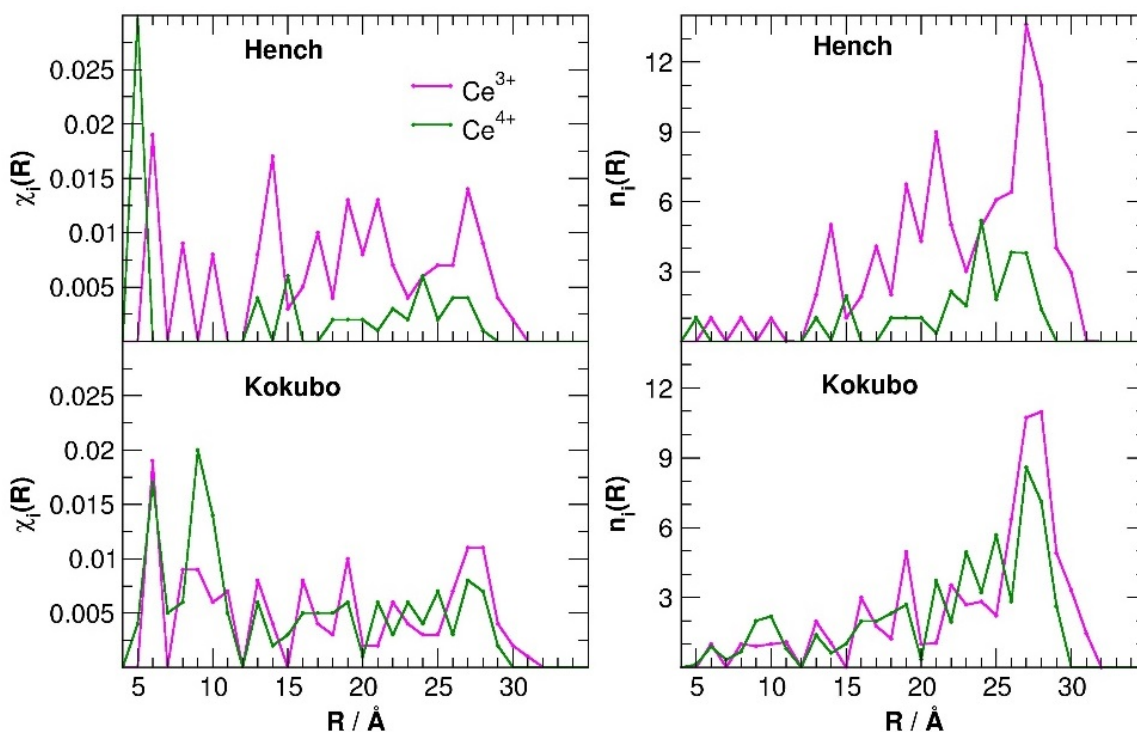


Figure 3: Fraction of Ce cations as functions of the distance from the center of mass in Ce-BG and Ce-K NPs.

1 \AA , located at distance $(R \pm \Delta R)$ from the centre of mass. The atomic fraction and density in each shell were calculated as $\chi_i(R) = n_i(R)/N(R)$ and $\rho_i(R) = n_i(R)/V(R)$ where n_i and N are the time-averaged number of atoms of species i and of all species found in the shell, respectively, while V is the volume of the shell.

The fraction and density profiles show that near the surface (*i.e.* $R > 28 \text{\AA}$) there is a sudden increase in the

content of Na cations for both types of NPs. The Na population is slightly larger in the Ce-K NP surface in comparison to the Ce-BG NP one. Overall, the exposed surface is 5–6 \AA thick and mainly composed of O and Na, as well as depleted in Si, P and Ca.

The changes in the atomic fraction and total number of cerium cations with the distance R are reported in Figure 3.

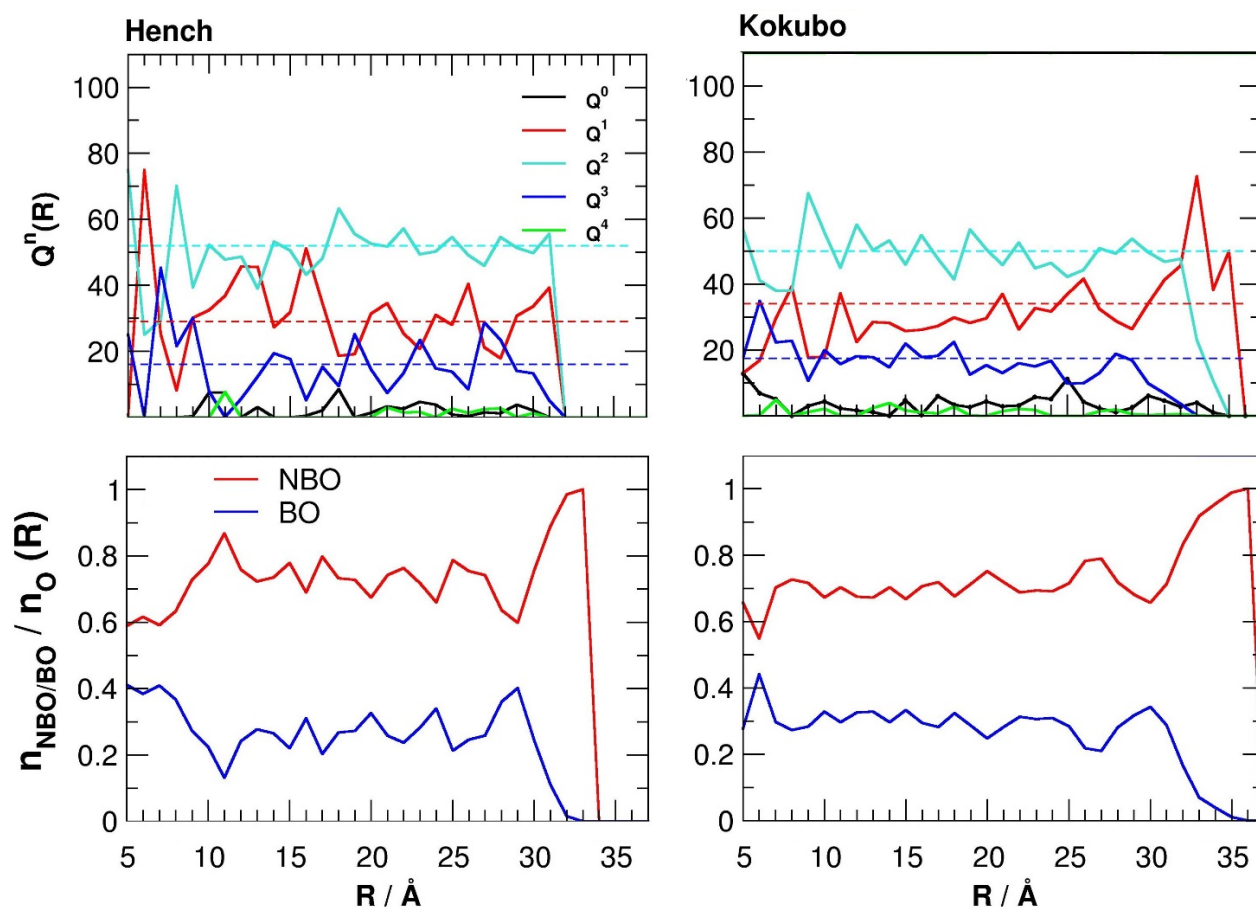


Figure 4: Distribution of Q^n silicate species (top panels) and NBO and BO relative fractions (bottom panels) going from the inner to the external (surface) regions of the Ce-BG and Ce-K NPs. Dashed lines mark the corresponding distributions in the bulk.

In the Ce-BG bulk glass, the ratio between Ce^{3+} and Ce^{4+} content is about ~ 3.5 ; almost the same ratio is found in the core region ($0 < R < 28$ Å) of the Ce-BG NP, whereas on the NP surface the Ce^{3+} / Ce^{4+} ratio is almost 13, denoting an almost exclusive presence of Ce^{3+} .

The Ce-K NP displays a rather different ratio between the two oxidation states of Ce: in the core region the ratio Ce^{3+} / Ce^{4+} is ~ 1.0 (similar to the bulk ratio of ~ 1.2), whereas on the surface region ($28 < R < 35$ Å) the ratio is ~ 2.1 , much smaller than the one observed on the surface of the Ce-BG NP. In other words, the surface of the Ce-K NP contains a significantly higher Ce^{4+} amount than the Ce-BG NP.

Thus, in line with the results obtained by Pirmohamed *et al.*,¹² who compared the catalase mimetic activity of ceria NPs with different Ce^{3+}/Ce^{4+} ratios (from 6 to 26) and found the best results for systems with low ratios, the Ce-K NP should possess better antioxidant properties compared to conventional bioactive glasses.

Silicate network connectivity and NBO/BO distributions

The degree of polymerization of glasses and nano-glasses can be investigated in terms of silicate network connectivity. The variations of the Q^n (Si) species distributions (with n being the number of bridging oxygens bonded to Si) as a function of the distance from the center of the two NPs are shown in Figure 4.

The Q^2 , Q^1 and Q^3 species are the most abundant for both Ce-BG and Ce-K NPs. The radial profile of the Q^n distribution of the Ce-BG NP is different with respect to that previously reported for Ce-free BG NPs.²⁶ In the latter case, the fraction of chain-like Q^2 units does not markedly change at the surface, but the Q^1 and Q^3 curves intersect, reflecting a surface depleted of branched Q^3 units and enriched in Q^1 chain-end units. Instead, in Ce-BG NPs the Q^1 and Q^3 curves do not intersect at the surface because the amount of Q^1 species is greater than that of Q^3 species already in the bulk. The Ce-BG bulk glass consists of 29.2% Q^1 , 52.0% Q^2 and 15.9% Q^3 species, whereas the Ce-free

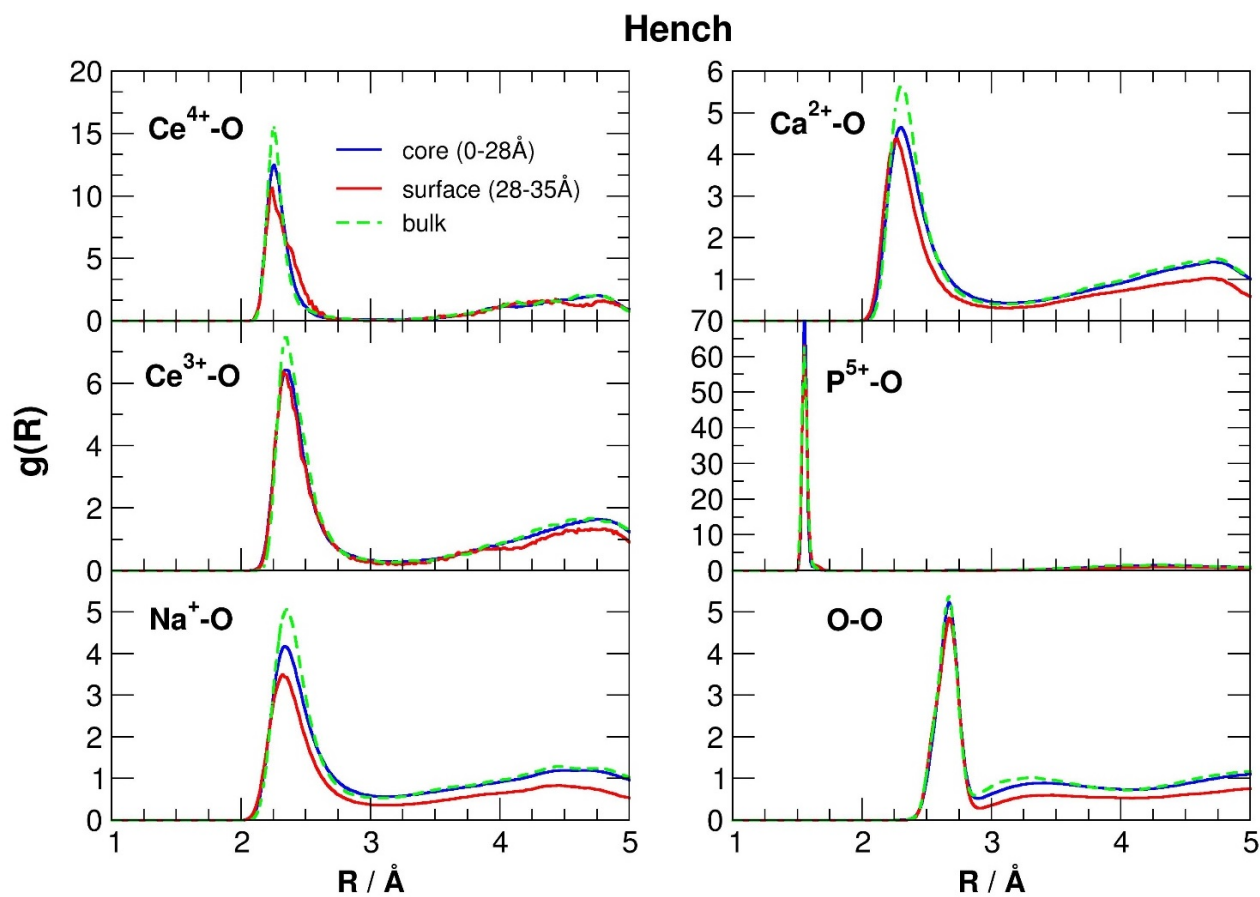


Figure 5: Pair radial distribution functions, $g(r)$, for the X-O pairs (where X = P, Na, Ca, Ce^{3+} and Ce^{4+}) calculated in the inner core ($0 \text{ \AA} < R < 28 \text{ \AA}$) and on the outer surface ($28 \text{ \AA} < R < 33 \text{ \AA}$) of the Hench NP; the $g(r)$'s of the bulk glass (dashed green line) are also shown.

BG bulk glass comprises 19.2% Q^1 , 52.0% Q^2 and 25.9% Q^3 species.

On the other hand, for the Ce-K NP the curves corresponding to Q^1 and Q^2 species intersect at the surface, where the structure is dominated by Q^1 species instead of Q^2 species as in the bulk.

The average silicate network connectivity in the surface region (calculated from the Q^n fractions there) turns out to be 1.8 and 1.7 for Ce-BG and Ce-K NPs, respectively, compared to 2.0 and 1.8 in the bulk.

The bottom panels of Figure 4 show the fraction of NBO and BO as a function of the distance from the centre of the particle: a large excess of non-bridging oxygens is present on the NP surface with respect to the bulk. The excess of NBOs appears as the driving force behind sodium enrichment in the surface of NPs, since the negative charges born by NBOs are stabilized by the migration of mobile sodium cations in the outermost regions, as reported also in other investigations [32].

Coordination shell of modifier cations

The short-range structure of both glass NPs has been characterized in terms of pair radial distributions functions, $g(r)$, which give insight into the network of bonds inside the material. The $g(r)$ functions were computed for two spherical regions, one with radius spanning from 0 to 28 \AA representing the core structure of the NPs, and one from 28 to 34 \AA that represents the surface.

Figures 5 and 6 shows the distributions obtained for the X-O pairs (where X = Si, Na, Ca, Ce^{3+} and Ce^{4+}) for the Ce-BG and Ce-K NPs, respectively. The $g(r)$ of the bulk structures for both glass compositions are also reported for comparison.

As previously found for a Ce-free BG NP [26], the good match between the $g(r)$ computed for bulk, core and surface of the particles suggests that the characteristic nearest-neighbours distances are not significantly affected by reducing the size of the system. Some differences emerge in the peak heights, which have a slightly lower intensity in the surface region. This essentially reflects the

Table 3: Average X-O coordination numbers ($X = \text{Ce}^{3+/4+}$, Ca, Na) in the bulk glass, and in the NP's core and surface.

X-O	Ce-BG			Ce-K		
	bulk	core	surface	bulk	core	surface
Ca-O	5.9	5.7	4.8	5.7	5.5	4.8
Na-O	6.0	5.8	4.3	5.8	5.6	4.3
Ce^{3+} -O	6.6	6.6	5.7	6.3	6.3	6.1
Ce^{4+} -O	7.1	7.0	-	6.8	6.7	6.6

The cut-off used are 3.0, 3.1 and 3.5 for Ca-O, Na-O and Ce-O pairs.

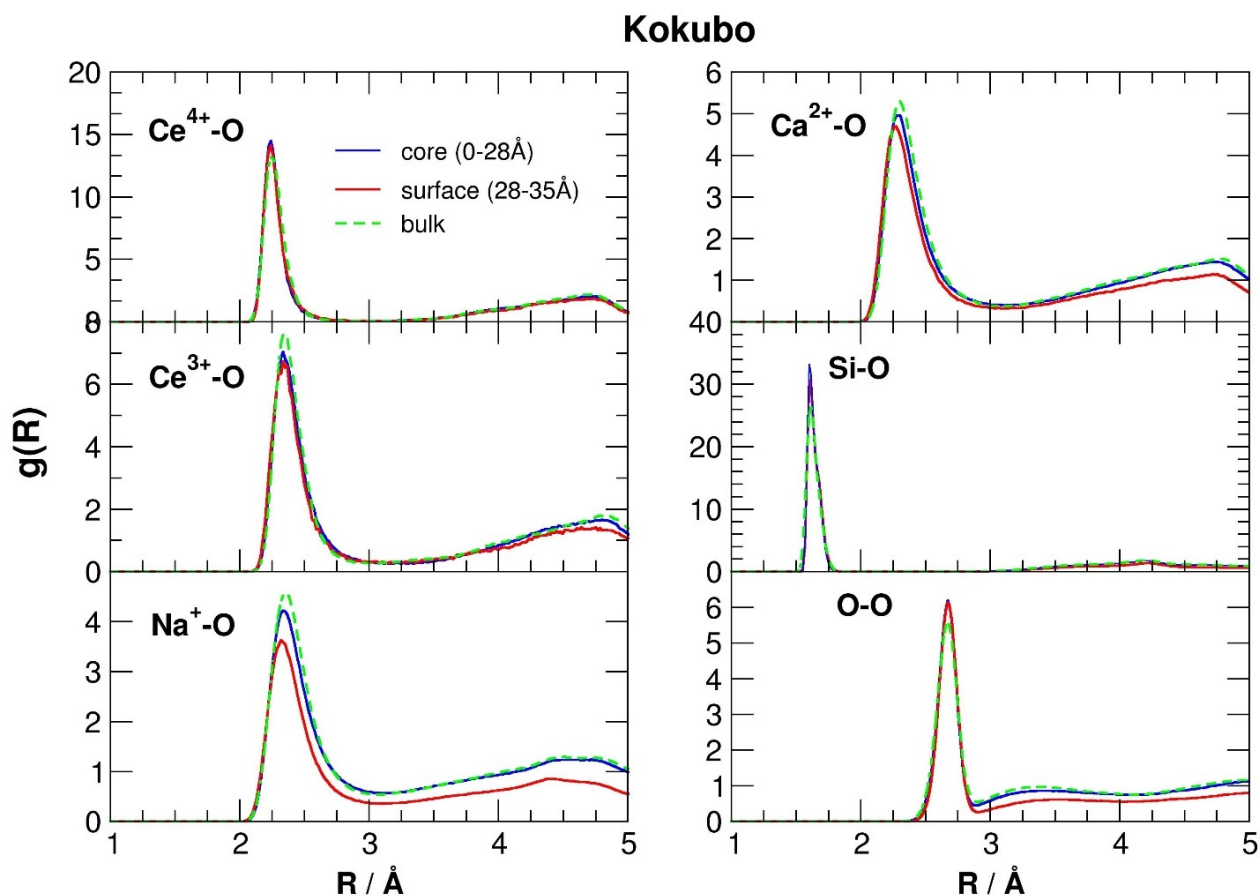


Figure 6: Radial distribution functions, $g(r)$, for the X-O pairs (where $X = \text{Si}, \text{Na}, \text{Ca}, \text{Ce}^{3+}$ and Ce^{4+}) calculated in the inner core ($0 \text{ \AA} < R < 28 \text{ \AA}$) and on the outer surface ($28 \text{ \AA} < R < 33 \text{ \AA}$) of the Kokubo NP; the $g(r)$'s of the bulk glass (green dashed line) are also shown.

empty external region outside the nanoparticle that leads to a reduced coordination number of the cations exposed on the surface. The $g(r)$'s computed in the inner region are very similar to their bulk counterparts, denoting full recovery of the bulk-like structure already below 5–6 Å under the nanoparticle boundary, in close agreement with the behaviour found for the MD models of a 45S5 NP of similar size to the present ones [26]. This agreement seems to denote that cerium doping does not significantly perturb the short-range structure of the glass nanoparticles.

Table 3 reveals that the average number of oxygen atoms $n(r_c)$ around sodium, calcium, and cerium is systematically reduced from bulk and inner core to surface of the NPs. In particular, $n(r_c)$ around sodium is reduced from 5.8 in the core to 4.3 in the surface of the Ce-BG NP and from 5.6 in the core to 4.3 in the surface of the Ce-K NP. The average coordination number of calcium is reduced from 5.7 to 4.8 and from 5.5 to 4.8 for the Ce-BG and Ce-K NPs, respectively.

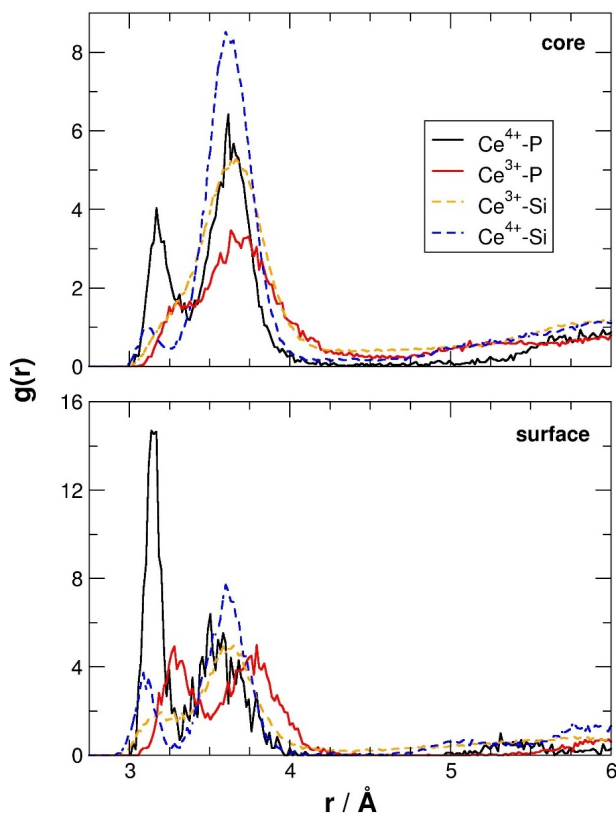


Figure 7: Pair radial distribution functions, $g(r)$, of Ce atoms calculated in the inner core ($0 \text{ \AA} < R < 28 \text{ \AA}$) and on the outer surface ($28 \text{ \AA} < R < 33 \text{ \AA}$) of the Hench nanoparticle.

Turning to cerium ions, the Ce^{3+} -O coordination numbers decrease from 6.6 (6.3) in the bulk to 5.7 (6.1) at the surface in the Ce-BG (K) NPs. Because of the very small quantity of Ce^{4+} found at the surface of the Ce-BG NP, the corresponding coordination numbers are not reported.

These variations demonstrate that the most exposed modifier cations, which turn out to be those with smaller charges (sodium and calcium), undergo a more marked depletion in their oxygen coordination shell and thus are unable to complete the ideal pseudo-octahedral coordination observed for Na and Ca in the bulk. Consequently, sodium ions exposed at the NP surfaces will have a more pronounced Lewis acidity with respect to those in the bulk and thus they are expected to be very reactive in the physiological environment.

In analogy, also the reduced number of oxygen ions coordinated to Ce ions exposed at the surface have a great impact on the antioxidant properties of such glass nanoparticles since the catalytic activity of under-coordinated Ce ions should be much higher than that of fully coordinated ions buried in the glass matrix.

Cerium second coordination sphere

In a previous paper [18], we have shown that the different $\text{Ce}^{3+}/\text{Ce}^{4+}$ ratio found in the bulk of the investigated glasses is correlated with the presence of phosphate groups. In particular, we showed that in phosphate-free glasses Ce is coordinated by non-bridging oxygens belonging to the silicate network, whereas in phosphate-containing glasses the NBOs around Ce ions come from orthophosphate groups. The latter groups seem to stabilize Ce^{3+} species subtracting it from the interconversion process between Ce^{3+} and Ce^{4+} , which is of fundamental importance for the exhibition of the catalase mimetic activity.

In order to confirm these results also on nano-sized systems we have analyzed the second coordination sphere around Ce^{3+} and Ce^{4+} ions in the Ce-BG NP since in this system both silicate and orthophosphate groups are present. The Ce-Si/P pair distribution functions reported in Figure 7 reveal that both Ce-P and Ce-Si PDFs present a double peak centered at 3.1–3.2 and 3.5–3.6 Å depending on the Ce oxidation state. The Ce-P PDFs exhibit a short-distance peak more pronounced than the second one, whereas the opposite is observed for the Ce-Si pair, meaning that cerium is found at shorter distances from P than Si.

The calculation of the Ce-P and Ce-Si coordination numbers shows that the latter are greater than the former. However, this is a consequence of the very high amount of silicon with respect to phosphorous in the system and does not denote preference of Ce for Si. To determine if Ce has a different affinity to Si or P we have normalized the $\text{CN}(\text{Ce-Si})/\text{CN}(\text{Ce-P})$ ratio with respect to the total number of Si and P atoms in the simulation box. When the ratio $R_{\text{Ce}}^{\text{Si/P}} = \frac{\text{CN}(\text{Ce-Si})}{\text{CN}(\text{Ce-P})} \times \frac{n^{\circ}\text{P}}{n^{\circ}\text{Si}}$ (where $n(\text{P})$ and $n(\text{Si})$ represent the number of P and Si atom in the models, respectively) is > 1 , Ce has a greater affinity to Si, whereas when the ratio is < 1 Ce favors P coordination. These ratios are 0.44 and 0.90 for Ce^{3+} and Ce^{4+} on the surface, confirming the preference of Ce to coordinate orthophosphate groups than silicate ones.

4 Conclusions

The enhanced antioxidant properties of Ce-K NP with respect to Ce-BG NP has been investigated by means of classical core-shell molecular dynamics simulations. We have shown that the different catalase mimetic activity of the two compositions is related to the $\text{Ce}^{3+}/\text{Ce}^{4+}$ ratio exposed at the NP surface. Ce-K NP possesses a lower ratio (2.1)

with respect to Ce-BG NP (13). The surface of the Ce-BG NP is mainly populated by Ce^{3+} ions with a high affinity for orthophosphate units, which can stabilize this oxidation state. The formation of cerium phosphate domains reduces the catalase mimetic activity of Ce-BG compared to Ce-K nanoparticles, since both Ce^{3+} and Ce^{4+} ions are necessary for the catalysis of the dismutation reaction of hydrogen peroxides.

Moreover, our simulations reveal that cerium sites in proximity of the surface are under-coordinated and thus with high Lewis acidity and prone to quickly react with hydrogen peroxide and other species present in physiological environments, thus accelerating the catalytic activity of Ce-containing glass NPs.

Acknowledgement: A. Tilocca gratefully acknowledges support from the UK's Royal Society (University Research Fellowship). The authors acknowledge the contribution of Dr. Elisa Gambuzzi.

References

- [1] Hench L. L., *Bioceramics*. *J. Am. Ceram. Soc.* 1998, 81(7), 1705–1728.
- [2] Jones J. R., [Review of Bioactive Glass: From Hench to Hybrids](#). *Acta Biomater.* 2013, 9(1), 4457–4486.
- [3] Hench L. L., Splinter R. J., Allen W. C., Greenlee T. K., *Bonding Mechanisms at the Interface of Ceramic Prosthetic Materials*. *J. Biomed. Mater. Res.* 1971, 5(6), 117–141.
- [4] Xynos I. D., Edgar A. J., Buttery L. D. K., Hench L. L., Polak J. M., *Gene-Expression Profiling of Human Osteoblasts Following Treatment with the Ionic Products of Bioglass (R) 45S5 Dissolution*. *J. Biomed. Mater. Res.* 2001, 55(2), 151–157.
- [5] Hench L. L., Polak J. M., *Third-Generation Biomedical Materials*. *Science* 2002, 295(5557), 1014–1017.
- [6] Brunner T. J., Grass R. N., Stark W. J., *Glass and Bioglass Nanopowders by Flame Synthesis*. *Chem. Commun.* 2006, No. 13, 1384–1386.
- [7] Loher S., Reboul V., Brunner T. J., Simonet M., Dora C., Neuenchwander P., Stark W. J., *Improved Degradation and Bioactivity of Amorphous Aerosol Derived Tricalcium Phosphate Nanoparticles in Poly(lactide-Co-Glycolide)*. *Nanotechnology* 2006, 17(8), 2054.
- [8] Vollenweider M., Brunner T. J., Knecht S., Grass R. N., Zehnder M., Imfeld T., Stark W. J., [Remineralization of Human Dentin Using Ultrafine Bioactive Glass Particles](#). *Acta Biomater.* 2007, 3(6), 936–943.
- [9] Lin S., Van den Bergh W., Baker S., Jones J. R., *Protein Interactions with Nanoporous Sol-Gel Derived Bioactive Glasses*. *Acta Biomater.* 2011, 7(10), 3606–3615.
- [10] Boccaccini A. R., Erol, M., Stark W. J., Mohn D., Hong Z., Mano J. F., *Polymer/bioactive Glass Nanocomposites for Biomedical Applications: A Review*. *Compos. Sci. Technol.* 2010, 70(13), 1764–1776.
- [11] Kumar A., Das S., Munusamy P., Self W., Baer D. R., Sayle D. C., Seal S., *Behavior of Nanoceria in Biologically-Relevant Environments*. *Environ. Sci. Nano* 2014, 1(6), 516–532.
- [12] Pirmohamed T., Dowding J. M., Singh S., Wasserman B., Heckert E., Karakoti A. S., King J. E. S., Seal S., Self W. T., *Nanoceria Exhibit Redox State-Dependent Catalase Mimetic Activity*. *Chem. Commun.* 2010, 46(16), 2736–2738.
- [13] Celardo I., Pedersen J. Z., Traversa E., Ghibelli L., *Pharmacological Potential of Cerium Oxide Nanoparticles*. *Nanoscale* 2011, 3(4), 1411–1420.
- [14] Nicolini V., Gambuzzi E., Malavasi G., Menabue L., Menziani M. C., Lusvardi G., Pedone A., Benedetti F., Luches P., D'Addato S., Valeri S., *Evidence of Catalase Mimetic Activity in $\text{Ce}^{3+}/\text{Ce}^{4+}$ Doped Bioactive Glasses*. *J. Phys. Chem. B* 2015, 119(10), 4009–4019.
- [15] McCormack R. N., Mendez P., Barkam S., Neal C. J., Das S., Seal S., *Inhibition of Nanoceria's Catalytic Activity due to Ce^{3+} Site-Specific Interaction with Phosphate Ions*. *J. Phys. Chem. C* 2014, 118(33), 18992–19006.
- [16] Leonelli C., Lusvardi G., Malavasi G., Menabue L., Tonelli M., [Synthesis and Characterization of Cerium-Doped Glasses and in Vitro Evaluation of Bioactivity](#). *J. Non-Cryst. Solids* 2003, 316(2–3), 198–216.
- [17] Kokubo T., *Surface Chemistry of Bioactive Glass-Ceramics*. *J. Non-Cryst. Solids* 1990, 120(1–3), 138–151.
- [18] Nicolini V., Varini E., Malavasi G., Menabue L., Menziani M. C., Lusvardi G., Pedone A., Benedetti F., Luches P., *The Effect of Composition on Structural, Thermal, Redox and Bioactive Properties of Ce-Containing Glasses*. *Mater. Des.* 2016, 97, 73–85.
- [19] Misra S. K., Mohn D., Brunner T. J., Stark W. J., Philip S. E., Roy I., Salih V., Knowles J. C., Boccaccini A. R., *Comparison of Nanoscale and Microscale Bioactive Glass on the Properties of P(3HB)/Bioglass® Composites*. *Biomaterials* 2008, 29(12), 1750–1761.
- [20] Misra S. K., Nazhat S. N., Valappil S. P., Moshrefi-Torbati M., Wood R. J. K., Roy I., Boccaccini A. R., *Fabrication and Characterization of Biodegradable Poly(3-Hydroxybutyrate) Composite Containing Bioglass*. *Biomacromolecules* 2007, 8(7), 2112–2119.
- [21] Hoang V. V., *Molecular Dynamics Simulation of Amorphous SiO_2 Nanoparticles*. *J. Phys. Chem. B* 2007, 111(44), 12649–12656.
- [22] Tilocca A., [Current Challenges in Atomistic Simulations of Glasses for Biomedical Applications](#). *Phys. Chem. Chem. Phys.* 2014, 16(9), 3874–3880.
- [23] Smith W., Forester T. R., *DL_POLY_2.0: A General-Purpose Parallel Molecular Dynamics Simulation Package*. *J. Mol. Graph.* 1996, 14(3), 136–141.
- [24] Dick B., Overhauser A., *Theory of the Dielectric Constants of Alkali Halide Crystals*. *Phys. Rev.* 1958, 112(1), 90–103.
- [25] Tilocca A., [Short- and Medium-Range Structure of Multicomponent Bioactive Glasses and Melts: An Assessment of the Performances of Shell-Model and Rigid-Ion Potentials](#). *J. Chem. Phys.* 2008, 129(8), 084504.
- [26] Tilocca A., [Molecular Dynamics Simulations of a Bioactive Glass Nanoparticle](#). *J. Mater. Chem.* 2011, 21(34), 12660–12667.
- [27] Tilocca A., Cormack A. N., de Leeuw N. H., *The Structure of Bioactive Silicate Glasses: New Insight from Molecular Dynamics Simulations*. *Chem. Mater.* 2007, 19(1), 95–103.
- [28] Gambuzzi E., Pedone A., *On the Structure of Ce-Containing Silicophosphate Glasses: A Core-shell Molecular Dynamics Investigation*. *Phys. Chem. Chem. Phys.* 2014, 16(39), 21645–21656.

- [29] Pedone A., Menziani M. C., Cormack A. N., [Dynamics of Fracture in Silica and Soda-Silicate Glasses: From Bulk Materials to Nanowires](#). *J. Phys. Chem. C* 2015, 119(45), 25499–25507.
- [30] Pedone A., Properties Calculations of Silica-Based Glasses by Atomistic Simulations Techniques: A Review. *J. Phys. Chem. C* 2009, 113(49), 20773–20784.
- [31] Berendsen H. J. C., Postma J. P. M., van Gunsteren W. F., DiNola A., Haak J. R., Molecular Dynamics with Coupling to an External Bath. *J. Chem. Phys.* 1984, 81(8), 3684.
- [32] Corrales L. R., Du J., Characterization of Ion Distributions Near the Surface of Sodium-Containing and Sodium-Depleted Calcium Aluminosilicate Melts. *J. Am. Ceram. Soc.* 2006, 89(1), 36–41.